Structural basis for isoform-specific inhibition of human CTPS1

Eric M. Lynch[a], Michael A. DiMattia[b], Steven Albanese[b], Gydo C. P. van Zundert[b], Jesse M. Hansen[a], Joel D. Quispe[a], Madison A. Kennedy[a], Andreas Verras[b], Kenneth Borrelli[b], Angela V. Toms[c], Neelu Kaila[c], Kevin D. Kreutter[c], Joshua J. McElwee[c], and Justin M. Kollman[a,1]

[a]Department of Biochemistry, University of Washington, Seattle, WA 98195; [b]Schrödinger, New York, NY 10036; and [c]Nimbus Therapeutics, Cambridge, MA 02139

Edited by Edward H. Egelman, University of Virginia, Charlottesville, VA, and approved August 13, 2021 (received for review May 4, 2021)

Cytidine triphosphate synthase 1 (CTPS1) is necessary for an effective immune response, as revealed by severe immunodeficiency in CTPS1-deficient individuals [E. Martin *et al.*], [*Nature*] [510], [288–292] ([2014]). CTPS1 expression is up-regulated in activated lymphocytes to expand CTP pools [E. Martin *et al.*], [*Nature*] [510], [288–292] ([2014]), satisfying increased demand for nucleic acid and lipid synthesis [L. D. Fairbanks, M. Bofill, K. Ruckemann, H. A. Simmonds], [*J. Biol. Chem.*] [270], [29682–29689] ([1995]). Demand for CTP in other tissues is met by the CTPS2 isoform and nucleoside salvage pathways [E. Martin *et al.*], [*Nature*] [510], [288–292] ([2014]). Selective inhibition of the proliferative CTPS1 isoform is therefore desirable in the treatment of immune disorders and lymphocyte cancers, but little is known about differences in regulation of the isoforms or mechanisms of known inhibitors. We show that CTP regulates both isoforms by binding in two sites that clash with substrates. CTPS1 is less sensitive to CTP feedback inhibition, consistent with its role in increasing CTP levels in proliferation. We also characterize recently reported small-molecule inhibitors, both CTPS1 selective and nonselective. Cryo-electron microscopy (cryo-EM) structures reveal these inhibitors mimic CTP binding in one inhibitory site, where a single amino acid substitution explains selectivity for CTPS1. The inhibitors bind to CTPS assembled into large-scale filaments, which for CTPS1 normally represents a hyperactive form of the enzyme [E. M. Lynch *et al.*], [*Nat. Struct. Mol. Biol.*] [24], [507–514] ([2017]). This highlights the utility of cryo-EM in drug discovery, particularly for cases in which targets form large multimeric assemblies not amenable to structure determination by other techniques. Both inhibitors also inhibit the proliferation of human primary T cells. The mechanisms of selective inhibition of CTPS1 lay the foundation for the design of immunosuppressive therapies.

enzymes | CTP synthase | immune disorders | small molecules | cryo-EM

CTP synthase (CTPS) is a critical regulatory enzyme in nucleotide metabolism, catalyzing the rate-limiting step in de novo CTP synthesis. The two human CTPS isoforms, CTPS1 and CTPS2, share 75% sequence identity but have distinct physiological roles. While CTPS2 is uniformly expressed across various tissue types, CTPS1 expression is generally low but is up-regulated in activated T cells (1). Individuals deficient in CTPS1—owing to a deleterious homozygous mutation—are severely immunocompromised (1, 2). These individuals have T cells that fail to proliferate upon activation but lack other major clinical consequences, with demand for CTP in resting T cells and other tissues likely maintained by CTPS2 and the nucleoside salvage pathway (1). The proliferation of T cells from CTPS1-deficient individuals can be rescued by the addition of exogenous CTP (1). CTPS1 thus plays an essential role in expanding CTP pools in proliferating lymphocytes, where additional CTP is likely required to meet an increased demand for DNA, RNA, and membrane lipid biosynthesis (3). Selective inhibition of CTPS1 is therefore an attractive target for immunosuppressive therapies as well as the treatment of lymphocyte cancers, with potentially limited off-target effects. Existing CTPS inhibitors exhibit substantial toxicity (4, 5), and whether they have selectivity for CTPS isoforms is unknown.

CTPS is a homotetramer, with each monomer comprising a glutaminase domain and an amidoligase domain connected by an α-helical linker (6) (*SI Appendix*, Fig. S2*A*). The glutaminase domain hydrolyzes glutamine to produce ammonia, which is transferred to the amidoligase domain, where it is ligated to UTP to form CTP in an ATP-dependent process (*SI Appendix*, Fig. S2*A*). CTPS experiences feedback inhibition by CTP, which binds a site overlapping the UTP binding site and is allosterically regulated by GTP (7, 8) (*SI Appendix*, Fig. S2*A*). CTPS thus has the capacity to integrate information about the levels of all four major ribonucleotides. Substrate and product binding control a conserved conformational cycle in CTPS; the tetramer interface adopts a compressed or extended conformation in order to accommodate CTP or UTP binding, respectively (9, 10) (*SI Appendix*, Fig. S2 *B* and *C*). Furthermore, upon substrate binding, the glutaminase domain rotates relative to the amidoligase domain (*SI Appendix*, Fig. S2 *D* and *E*), opening a tunnel that likely facilitates ammonia transfer between the two active sites (6, 9, 10, 11). Polymerization into filaments adds another layer to CTPS regulation, which varies among species and between the human isoforms (9, 10, 12, 13). *Escherichia coli* CTPS polymerizes into inactive filaments in

Significance

An effective immune response depends on the proliferation of T cells, a process that requires the enzyme CTP synthase 1 (CTPS1). Individuals lacking CTPS1 due to a rare genetic disorder exhibit severe immunodeficiencies but lack other major clinical consequences; the requirement for CTP synthase outside of the immune response is met by a second isoform, CTPS2. Inhibiting CTPS1 without affecting CTPS2 is therefore a promising strategy for treating autoimmune disorders and T cell cancers while avoiding off-target effects. We characterize both CTPS1-selective and nonselective inhibitors. Structures of CTPS bound to inhibitors reveal the mechanisms of inhibition and CTPS1 selectivity. Differences in product feedback inhibition between CTPS1 and CTPS2 explain how CTPS1 may sustain enzymatic activity required for T cell proliferation.

Author contributions: E.M.L., M.A.D., S.A., G.C.P.v.Z., J.M.H., M.A.K., A.V., K.B., A.V.T., N.K., K.D.K., J.J.M., and J.M.K. designed research; E.M.L., M.A.D., S.A., G.C.P.v.Z., J.M.H., J.D.Q., and M.A.K. performed research; E.M.L., M.A.D., S.A., G.C.P.v.Z., J.M.H., M.A.K., A.V., K.B., A.V.T., N.K., K.D.K., J.J.M., and J.M.K. analyzed data; and E.M.L. and J.M.K. wrote the paper.

Competing interest statement: M.A.D, S.A., G.C.P.v.Z, A.V., and K.B. are employees of Schrödinger. A.V.T., N.K., K.D.K., and J.J.M. are employees of Nimbus Therapeutics.

This article is a PNAS Direct Submission.

[1]To whom correspondence may be addressed. Email: jkoll@uw.edu.

This article contains supporting information online at https://www.pnas.org/lookup/suppl/doi:10.1073/pnas.2107968118/-/DCSupplemental.

Published September 28, 2021.

the presence of CTP (12). Both human isoforms assemble filaments of stacked tetramers through conserved intertetramer interactions but with different functional consequences: CTPS1 polymerizes into filaments with increased activity upon substrate binding (9), whereas CTPS2 filaments dynamically switch between substrate- and product-bound conformations to produce highly cooperative regulation (10). CTPS filaments are observed under conditions of cellular stress, at particular stages of development, and in cancer cells, suggesting they are involved in adapting to changes in metabolic requirements (14–18).

The biochemical basis for the different physiological roles of CTPS1 and CTPS2 remains unclear. Here, we investigate the differential regulation of CTPS1 and CTPS2 by CTP and find that CTPS1 is active at higher CTP concentrations, consistent with its critical role in expanding nucleotide pools in proliferating cells. We also identify a second inhibitory CTP binding site that overlaps the CTPS ATP binding site. Furthermore, we show that a family of recently described small-molecule CTPS inhibitors binds in a site adjacent to the second CTP site and selectively targets CTPS1 through a mechanism dependent on a single amino acid substitution.

Results

CTPS1 Resists Feedback Inhibition by CTP. We investigated the regulation of human CTPS1 and CTPS2 by CTP and found that the half maximal inhibitory concentration (IC_{50}) for CTPS1 was roughly 5× greater than for CTPS2 (Fig. 1*A* and *SI Appendix*, Table S1). This resistance to CTP inhibition likely reflects the isoform-specific role of CTPS1 in expanding CTP pools during proliferation. Notably, the activity of CTPS2 was roughly twofold higher than CTPS1 (*SI Appendix*, Fig. S1*A*), likely because CTPS1 activity is increased roughly sixfold by polymerization into filaments (9), while assays here were performed at concentrations where very few CTPS filaments are observed (10) (*SI Appendix*, Fig. S1*B*). Toward understanding the structural basis for this differential regulation, we improved our previously determined product-bound CTPS2 filament structure (10); applying recent advances in cryo-electron microscopy (cryo-EM) image processing, including Bayesian polishing, optics refinement, and density modification, improved the resolution from 3.1 to 2.8 Å. (Fig. 1*B*, *SI Appendix*, Figs. S3 and S4*A*). This revealed CTP bound to two sites on CTPS2: one CTP in the canonical inhibitory site (site 1), which overlaps partially with the UTP binding site, and another in a site (site 2), which overlaps partially with the ATP binding site (Fig. 1 *C*–*F*). Both ADP and CTP were present in the CTPS2 cryo-EM sample, and we previously modeled the nucleotide in site 2 as ADP (10). However, the improved resolution of the current structure clearly revealed that this nucleotide is instead CTP, with density observed for three phosphates and a pyrimidine base (*SI Appendix*, Fig. S4*B*). A 3.6-Å structure of CTPS2 solved in the presence of CTP alone confirmed that CTP binds to both sites (*SI Appendix*, Fig. S4 *C*–*E*). Similarly, a recent study identified CTP in both sites 1 and 2 in a cryo-EM structure of CTP-bound *Drosophila melanogaster* CTPS (19). CTP can therefore inhibit CTPS by competing for binding of both UTP and ATP at sites 1 and 2, respectively, perhaps allowing CTPS to respond to changes in the relative balance of nucleotide levels. CTP has not been observed in site 2 in existing crystal structures of CTP-bound *E. coli* CTPS (8, 9), likely due to various amino acid substitutions in the *E. coli* enzyme, including K306, which is likely to clash with CTP (*SI Appendix*, Fig. S4*F*).

There is no existing structure of inhibited, CTP-bound CTPS1, which is predominantly in a tetrameric form (9, 10). To determine if structural differences account for the increased CTP IC_{50} of CTPS1 over CTPS2, we determined the cryo-EM structure of free CTPS1 tetramers bound to CTP at 6.2-Å resolution (*SI Appendix*, Figs. S5 and S6). For structure determination, we used CTPS1 with the previously characterized C-terminal truncation and H355A nonpolymerizing mutations (9, 10), which reduced nonspecific aggregation in cryo-EM samples without affecting tetramer formation (*SI Appendix*, Fig. S5). The overall conformation of CTP-bound CTPS1 resembles existing CTP-bound CTPS structures (8, 9, 10): the tetramer interface adopts a characteristic compressed conformation (*SI Appendix*, Fig. S6*B*), and the glutaminase domains are rotated away from the amidoligase domains, separating the two active sites within each monomer (*SI Appendix*, Fig. S6 *C* and *D*). The glutaminase domains of CTP-bound CTPS1 exhibited an additional, much smaller rotation in a roughly perpendicular direction (*SI Appendix*, Fig. S6*E*). CTP was bound to both sites 1 and 2 in CTPS1 (*SI Appendix*, Fig. S6*F*). While site 1 is completely conserved between the two isoforms, site 2 has a single difference: residue T250 in CTPS2, which is

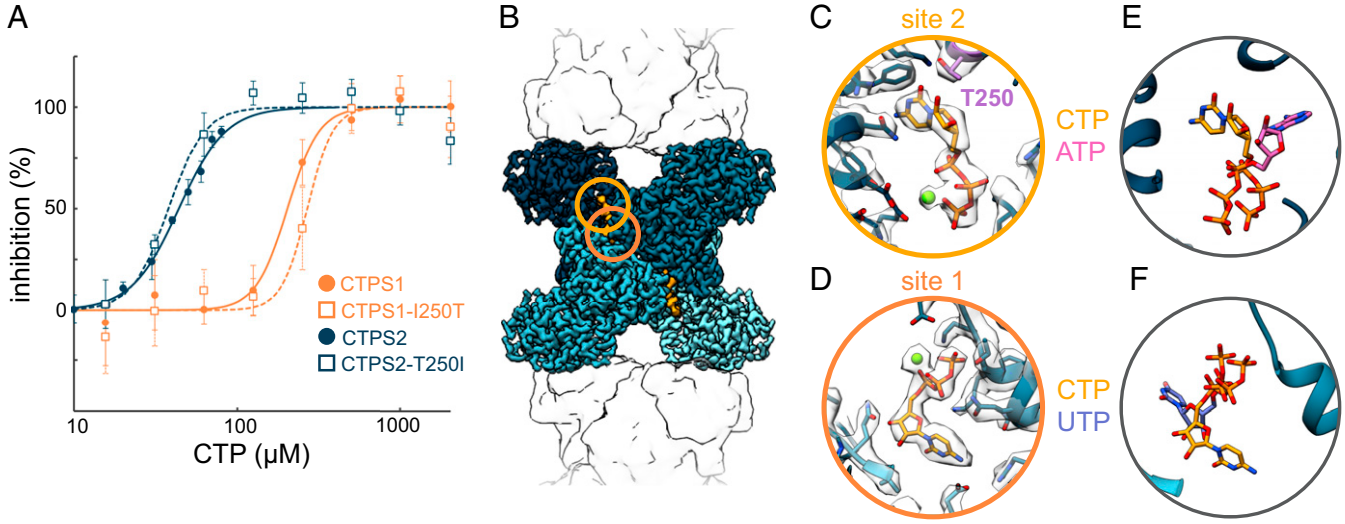

Fig. 1. CTPS1 has a higher CTP IC_{50} than CTPS2. (*A*) CTP inhibition curves for wild-type and mutant CTPS1 and CTPS2 measured by ADP-Glo. CTPS1 resists inhibition by CTP compared with CTPS2. (*B*) 2.8-Å cryo-EM structure of CTPS2 bound to CTP. (*C* and *D*) Zoomed-in views of the circles in (*B*) showing CTP bound to site 2 (*C*) and site 1 (*D*). The position of residue T250 is indicated in panel *C*. Magnesium ions are colored green. (*E*) Site 2 CTP overlaps with the ATP binding site. (*F*) Site 1 CTP overlaps with the UTP binding site. Data shown in graphs are mean and SD of $n = 3$ technical replicates.

adjacent to the CTP base, is substituted for I250 in CTPS1 (Fig. 1*C*). We tested whether the identity of residue 250 might account for the differences in CTP IC_{50} between isoforms by swapping this residue in CTPS1-I250T and CTPS2-T250I mutants. This had no substantial effect on CTP IC_{50} values compared to the wild-type proteins (Fig. 1*A*). The increased CTP IC_{50} of CTPS1 relative to CTPS2 is therefore not explained by gross conformational differences or changes in primary sequence at the CTP binding sites but may instead arise from more subtle differences in the stability of the CTP-bound conformation between the two isoforms.

To determine whether active state CTPS1 and CTPS2 are also in the same conformation, we solved the structure of the CTPS1 filament bound to UTP, glutamine, and the nonhydrolyzable ATP analog AMPPNP at 2.8-Å resolution, providing a high-resolution structure of CTPS bound to all three substrates (Fig. 2, *SI Appendix*, Figs. S3 and S7*A*). Tetramers from the active-state CTPS1 filament structure were in the same conformation as tetramers from our previous active-state CTPS2 filament structure (10) (C-α RMSD: 0.9 Å) (Fig. 2*C*).

Selective Small-Molecule Inhibition of CTPS1. A family of potent CTPS inhibitors was recently disclosed (20–23), a subset of which exhibit strong selectivity for CTPS1 over CTPS2. However, how these compounds bind, how they inhibit, and how they distinguish between isoforms has been unclear. We selected a variety of CTPS1-selective and CTPS1/CTPS2-nonselective inhibitors and determined IC_{50} values against both human CTPS isoforms. Nonselective inhibitors had similar nanomolar affinities for both isoforms, while the selective inhibitors exhibited CTPS1 selectivity of 2 to 3 orders of magnitude (Fig. 3*A*, *SI Appendix*, Fig. S7 *B* and *C* and Table S1).

To investigate the mechanism of inhibition, we determined cryo-EM structures of both CTPS isoforms bound to either the selective R80 or nonselective T35 inhibitor (*SI Appendix*, Fig. S7*B*) in addition to substrates UTP and glutamine (Fig. 3, *SI Appendix*, Fig. S7 *D–F*). Under these conditions, both CTPS1 and CTPS2 formed filaments, though final high-resolution (2.7 to 3.1 Å) structures were determined by masked refinements focused on single tetramers (*SI Appendix*, Figs. S3 and S7*E*). Binding modes of R80 and T35 were modeled by docking with GlideEM and subsequent refinement using Phenix/OPLS3e (24, 25). R80 and T35 bridge across the CTP site 2 and ATP binding sites without affecting binding of either UTP or glutamine (Fig. 3 *C* and *D*, *SI Appendix*, Fig. S7*G*). Both compounds form hydrogen bonds with sidechains R76, K319, and H323 as well as the backbone amide nitrogen of V247 (Fig. 3 *E–H*). Pi–pi and pi–cation interactions with Y251 and R217 were also observed (Fig. 3 *E–H*). The amide of T35 allows it to form an additional hydrogen bond with residue 250 and possibly S249, in contrast to the reverse amide in R80 (Fig. 3 *F* and *H*). The orientation of the pyridine ring was ambiguous at these resolutions and was modeled with the pyridine nitrogen oriented toward the nitrogen of the amide or reverse amide bond (Fig. 3 *E–H*). The precise orientation of the terminal cyclopropyl group was similarly ambiguous at these resolutions and varied across the structures (Fig. 3 *E–H*). The inhibitor-bound CTPS1 and CTPS2 structures were in the substrate-bound conformation, with extended tetramer interfaces and glutaminase domains rotated toward the amidoligase domains (Fig. 4). R80 and T35 therefore do not appear to function as allosteric inhibitors that alter the conformation of CTPS but instead as competitive inhibitors that prevent ATP binding.

We next investigated the mechanism of R80 selectivity. The amide or reverse amide bond near the center of the compounds sits adjacent to residue 250 (CTPS1 I250; CTPS2 T250) (Fig. 5*A*), and swapping this residue in CTPS1-I250T and CTPS2-T250I mutants was sufficient to invert the selectivity of R80 between the isoforms (Fig. 5*B* and *SI Appendix*, Fig. S8*A*). While the I250T substitution is highly conserved among vertebrates (outside of fish), residue 250 is an isoleucine in both CTPS1 and CTPS2 in rodents (*SI Appendix*, Fig. S8*B*), an important consideration for potential animal studies aimed at exploring this family of inhibitors. We therefore measured the inhibition of the mouse mCTPS1 and mCTPS2 isoforms by R80. As expected, mCTPS1 and mCTPS2 both exhibited nanomolar IC_{50} values for R80, comparable to human CTPS1 (Fig. 5*C*). Cryo-EM structures of mCTPS1, mCTPS2, and mutant mCTPS2-I250T filaments (2.4- to 2.8-Å resolution) showed R80 bound in the same site as the human enzymes (Fig. 5*D* and *SI Appendix*, Fig. S8 *C–G*). In addition, mCTPS2-I250T had a significantly increased IC_{50} for R80 compared with mCTPS1 and mCTPS2 (Fig. 5*C*). To test whether the role of residue 250 in determining selectivity is general to this family of inhibitors rather than specific to R80 and T35, we measured inhibition of mCTPS1, mCTPS2, and mCTPS2-I250T by several other selective and nonselective inhibitors (*SI Appendix*, Table S1). For all CTPS1-selective inhibitors, selectivity was not observed between the mCTPS1 and mCTPS2 isoforms but was restored by the mCTPS2-I250T mutant (*SI Appendix*, Table S1). This confirms that I250 is a key determinant of selectivity and suggests that precautions should be taken in interpreting the results of any mouse studies involving inhibitors targeting this binding pocket; candidate compounds for the selective inhibition of human CTPS1 would likely target both mouse CTPS isoforms, possibly leading to off-target effects, which could cause them to be unnecessarily dismissed based on an unrepresentative animal model.

Interestingly, the relative positions of the inhibitors and the loop containing residue 250 differed among the various structures (Fig. 5*E*). However, whether these differences contribute to the isoform selectivity of R80 is unclear; there was no apparent correlation between the position of this loop and the reduced affinity of R80 for CTPS2 and mCTPS2-I250T (Fig. 5*E*). Differences in solvation or other factors not observed at the resolution of these cryo-EM structures may further contribute to the selectivity of R80, in addition to the primary sequence variation at residue 250.

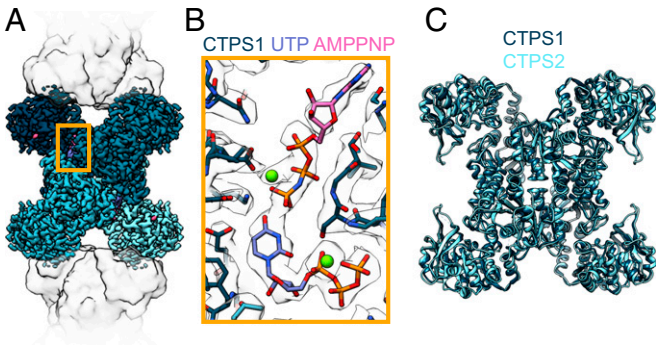

Fig. 2. Structure of the substrate-bound CTPS1 filament. (*A*) Cryo-EM structure of CTPS1 bound to UTP, glutamine, and AMPPNP. (*B*) Zoomed-in view of the yellow box in (*A*), showing UTP and AMPPNP in the active site. Magnesium ions are colored green. (*C*) Overlay of tetramers from substrate-bound CTPS1 and CTPS2 (PDB code: 6PK4) filaments, which are in the same conformation.

R80 and T35 Inhibit T Cell Proliferation. We next tested the ability of R80 and T35 to inhibit proliferation of Jurkat cells as well as cultured human and mouse primary T cells using the CellTiter-Glo assay. Both compounds effectively inhibited proliferation of all three lymphocyte cell lines, with nanomolar IC_{50} values comparable to those measured by in vitro enzyme assays (Fig. 6 *A–C* and *SI Appendix*, Table S2). Importantly, addition of exogenous

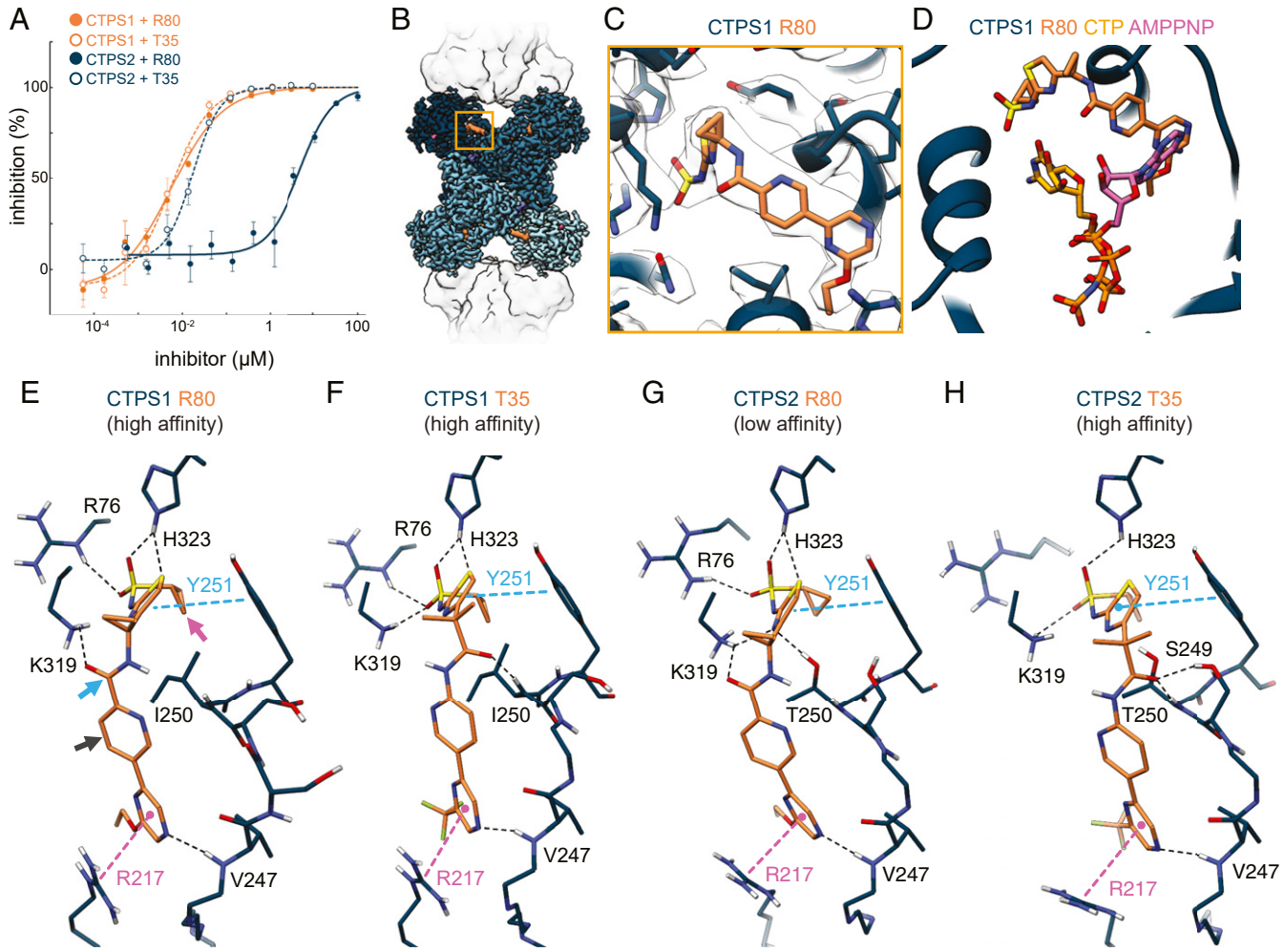

Fig. 3. Compound R80 is a potent selective inhibitor of CTPS1. (*A*) Inhibition curves for R80 and T35 against CTPS1 and CTPS2 measured by ADP-Glo. (*B*) Cryo-EM structure of CTPS1 bound to UTP, glutamine, and R80. (*C*) Zoomed-in view of the yellow box in (*B*) showing the R80 binding site. (*D*) Overlay of R80 with the CTP site 2 and ATP binding sites. The sites overlap. (*E*–*H*) Interaction diagrams for R80-bound CTPS1 (*E*), T35-bound CTPS1 (*F*), R80-bound CTPS2 (*G*), and T35-bound CTPS2 (*H*). Hydrogen bonds are shown as dashed black lines. Pi–pi and pi–cation interactions are shown as dashed blue and pink lines, respectively. The positions of the pyridine ring (gray arrow), amide, or reverse amide bond (blue arrow), and cyclopropyl group (pink arrow) are indicated in panel *E*. The orientation of the cyclopropyl group and pyridine ring varies among the structures. Data shown in graphs are mean and SD of $n = 2$ technical replicates from one representative experiment.

cytidine was sufficient to rescue proliferation through the nucleoside salvage pathway, indicating that the antiproliferative effect is specific to cytosine deprivation (Fig. 6 *A*–*C*). Similarly, exogenous CTP is sufficient to rescue the proliferation of T cells isolated from CTPS1-deficient individuals (1). R80 and T35 therefore appear to inhibit lymphocyte proliferation by preventing expansion of CTP pools via de novo synthesis by CTPS1, consistent with the potent inhibition of purified CTPS1 by both inhibitors (Fig. 6*D*). In vivo studies will be required to determine if the selectivity of R80 for CTPS1 prevents off-target toxicity. A variety of other selective and nonselective inhibitors similarly inhibited proliferation of cultured lymphocytes, typically with nanomolar IC_{50} values (*SI Appendix*, Table S2).

Discussion

Proliferating cells like activated lymphocytes have a high demand for ribonucleotides, in particular CTP and GTP (3, 26). Here, we have shown that CTPS1 has a reduced sensitivity to CTP feedback inhibition relative to CTPS2, which likely contributes to its role in expanding CTP pools in proliferating lymphocytes (1, 2). The observation that CTPS1 is critical to an effective immune response but otherwise nonessential makes it an ideal target for immunosuppression (1, 2). The CTPS1 R80 inhibitor characterized here is potent, highly selective for CTPS1 over CTPS2 in vitro, and effectively prevents the proliferation of cultured lymphocytes by depleting cytidine levels, making it a promising candidate for the development of immunosuppressive therapies. Nonetheless, further in vivo studies are required to determine the therapeutic potential of R80 and related compounds. Interestingly, R80 binds a site adjacent to binding site 2 of the native feedback inhibitor CTP, where it similarly precludes binding of the substrate ATP. Unlike CTP, however, R80 does not produce large conformational changes in CTPS relative to the substrate-bound conformation.

The rate-limiting step in GTP synthesis is catalyzed by inosine monophosphate dehydrogenase (IMPDH), and the proliferative IMPDH2 isoform appears to function in a manner analogous to CTPS1: IMPDH2 is up-regulated in proliferating cells (27–30) and resists feedback inhibition by GTP in order to expand GTP pools (31). The ability of IMPDH2 to resist GTP inhibition depends on its assembly into filaments (31), and filamentous structures of IMDPH have been observed in proliferative cancer cells,

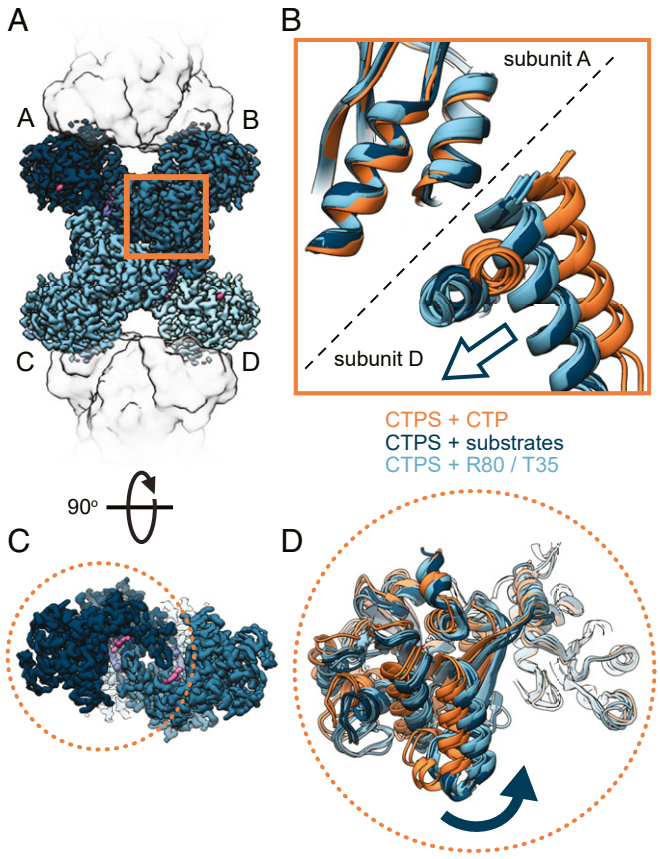

Fig. 4. R80- and T35-bound CTPS structures are in the substrate-bound conformation. (*A*) Cryo-EM structure of CTPS1 bound to UTP, glutamine, and R80. Subunits A to D of the tetramer are indicated. (*B*) Zoomed-in view of the orange box in (*A*), comparing the tetramer interface in substrate- and product-bound CTPS1 and CTPS2 to the R80- and T35-bound structures. (*C*) Top view of the structure shown in (*A*). (*D*) Zoomed-in view of the monomer circled in (*C*), comparing the glutaminase domain rotation of substrate- and product-bound CTPS1 and CTPS2 to the R80- and T35-bound structures. The inhibitor-bound structures are in the substrate-bound conformation.

pluripotent stem cells, and T cells (32–35). Whether CTPS similarly forms filaments in proliferating lymphocytes remains an open question of interest.

In addition to its role in the proliferation of healthy lymphocytes, CTPS is up-regulated in a variety of cancers (36–38) and has been a target for anticancer drugs for several decades. Existing inhibitors of CTPS are primarily metabolite analogs, which can produce a variety of undesirable off-target effects. Acivin, a naturally occurring glutamine analog that nonspecifically inhibits most glutaminases, inhibits CTPS through irreversible covalent modification of the glutaminase domain active site (39–41). However, acivicin failed as a cancer treatment in phase-II clinical trials, owing to significant neurological toxicity (4, 5). The pyrimidine analogs cyclopentenyl cytosine (CPEC) and 3-deazauridine inhibit CTPS and prevent cancer cell proliferation (42–46) and are particularly effective when used in combination with other cytidine analog drugs such as cytarabine and gemcitabine; CPEC and 3-deazauridine reduce CTP pools through inhibition of CTPS, thereby promoting the incorporation of cytidine analogs into DNA and inhibiting DNA synthesis (47–49). However, resistance to CPEC has been observed in cancer cells with adaptations that increase the activity of CTPS (50, 51). The CTPS1-specific inhibitor characterized here could prove useful as the basis for the treatment of cancer, perhaps avoiding the toxicity and drug-resistance adaptations associated with metabolite analogs targeting CTPS. However, further studies are warranted in order to determine whether R80 and related compounds can overcome the pitfalls associated with existing cancer therapeutics directed at CTPS.

Selective inhibition of CTPS1 may also be an effective strategy for fighting some infectious diseases. As with cancer cells, depleting CTP pools via CTPS inhibition enhances the efficacy of cytidine analogs in slowing the proliferation of HIV-infected cells (52). Furthermore, a recent study revealed that two SARS-CoV-2 proteins interact with and activate CTPS1 (53). Remarkably, in addition to providing CTP necessary for SARS-CoV-2 replication, activated CTPS1 also deamidates interferon regulatory factor 3, thus suppressing interferon production and inhibiting the innate immune response (53). Small-molecule CTPS inhibitors restore the innate immune response and suppress SARS-CoV-2 replication (53). However, whether these inhibitors are selective for CTPS1 is unclear. The potent, highly selective R80 CTPS1 inhibitor may therefore provide an effective means of suppressing the replication of SARS-CoV-2 and other pathogens that may hijack the de novo CTP synthesis pathway.

Cryo-EM is increasingly being recognized as a valuable technique in drug discovery, enabling the determination of protein structures not amenable to X-ray crystallography, including membrane proteins, dynamic and flexible assemblies, as well as large-scale filament complexes such as the CTPS filaments described here. As for CTPS, cryo-EM is likely to play an important role in drug discovery for other important therapeutic targets that also assemble metabolic filaments (31, 54–57). Importantly, cryo-EM also allows for the determination of structures in a variety of native conformational states free of the constraints of the crystal lattice; the R80- and T35-bound CTPS structures are in a substrate-bound conformation identified by cryo-EM (9, 10) but not observed in any existing CTPS structures solved by X-ray crystallography. Ongoing improvements to electron microscopes, detectors, automated data collection, and image processing continue to increase the quality and throughput of structures determined by cryo-EM, further establishing cryo-EM as a valuable asset for drug discovery pipelines (58, 59).

The R80- and T35-bound CTPS structures presented here provide a potential basis for structure-based design of CTPS inhibitors, providing the opportunity to further enhance specificity and potency. Future in vivo studies will be required to determine the efficacy of this family of inhibitors in treating human autoimmune disorders, cancer, and infectious diseases.

Materials and Methods

Preparation of Recombinant Human CTPS1 and CTPS2 from Yeast. Human CTPS1 and CTPS2 were purified from *Saccharomyces cerevisiae* strains GHY55 and GHY56 (60), as described previously (9, 10). The CTPS1-I250T and CTPS2-T250I mutants were generated by Q5 site-directed mutagenesis (NEB) and purified in the same manner as the wild-type proteins (*SI Appendix*, Fig. S9*A*).

Preparation of Recombinant Human CTPS1 and CTPS2. Human CTPS1 (Uniprot ID: P17812) and human CTPS2 (Uniprot ID: Q9NRF8) were codon optimized and cloned into a pFastBac expression vector with a C-terminal FLAG-His-Avi tag. Baculovirus was generated and amplified in Sf9 cells. Both human full-length proteins were expressed in Hi5 cells harvesting 48 h postinfection. The hCTPS1-FLAG-His-Avi protein was purified using a HiTrapFF column (GE Healthcare), eluted with 100 mM imidazole, and further purified with a 2-mL Pierce Anti-DYKDDDDK Affinity Resin column (Thermo Scientific). The hCTPS2-FLAG-His-Avi protein was purified using a HiTrapFF column (GE Healthcare), eluted with 100 mM imidazole, and further purified with a Superdex 200 26/600 column (GE Healthcare) (*SI Appendix*, Fig. S9*B*).

To generate a nonpolymerizing CTPS1 variant (9, 10), hCTPS1(1-558)-H355A was cloned into a pFastBac expression vector with a C-terminal His tag. Baculovirus was generated and amplified in Sf9 cells. The truncated mutant protein was expressed in Hi5 cells harvesting 48 h postinfection. The hCTPS1(1-558) H355A was purified using a HiTrapFF column (GE Healthcare), eluted with 250 mM imidazole, and further purified with Superdex 200 26/600 column (GE Healthcare) (*SI Appendix*, Fig. S9*B*).

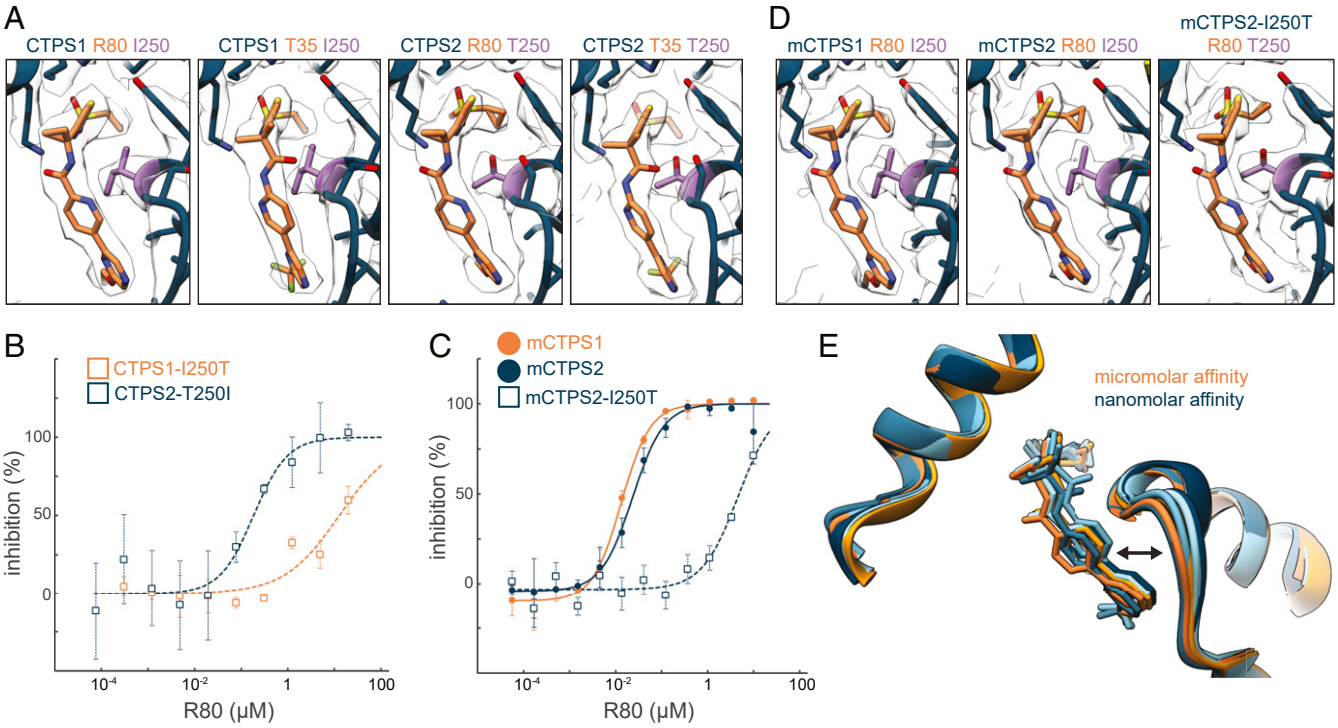

Fig. 5. Residue I250 determines the specificity of R80. (*A*) Structures of R80 and T35 bound to CTPS1 and CTPS2, with the positions of I250 and T250 indicated in purple. (*B*) Inhibition curves for R80 against the CTPS1-I250T and CTPS2-T250I swap mutants measured by ADP-Glo. (*C*) Inhibition curves for R80 against mCTPS1, mCTPS2, and mCTPS2-I250T measured by ADP-Glo. (*D*) Structures of R80 bound to mCTPS1, mCTPS2, and mCTPS2-I250T, with the positions of I250 and T250 indicated in purple. (*E*) Overlay of all human and mouse CTPS structures bound to R80 or T35. Structures with high- and low-affinity ligand binding are shown in shades of blue and orange, respectively. Data shown in graphs are mean and SD of $n = 3$ technical replicates for panel *B* and $n = 2$ technical replicates from one representative experiment for panel *C*.

Preparation of Recombinant Mouse CTPS1 and CTPS2. Mouse CTPS1 (Uniprot ID: P70698), mouse CTPS2 (Uniprot ID: P70303), and mouse CTPS2-I250T were codon optimized and cloned into a pCDNA3.1 transient transfection mammalian expression vector with a C-terminal FLAG-His-Avi tag. All mouse proteins were expressed in Expi293f cells in Expi293 media (ThermoScientific) for 72 h. The mCTPS1-FLAG-His-Avi protein was purified using nickel nitrilotriacetic acid (NiNTA) resin (Qiagen), eluted with 100 mM imidazole, and further purified with a 2-mL Pierce Anti-DYKDDDDK Affinity Resin column (Thermo scientific). The mCTPS2-FLAG-His-Avi wild-type and I250T proteins were purified using NiNTA resin (Qiagen), eluted with 100 mM imidazole, and further purified with a HiLoad 16/60 Superdex 200 column (GE Healthcare) (*SI Appendix*, Fig. S9*C*).

ADP-Glo Assays for CTPS Activity. Inhibition of CTPS by CTP, R80, and T35 was measured using the ADP-Glo assay (Promega). Assays using yeast-purified CTPS were performed in buffer containing 50 mM K-Hepes pH 8.0, 5 mM KCl, 0.01% Tween20, 0.01% bovine serum albumin (BSA), 20 mM $MgCl_2$, and 1 mM dithiothreitol (DTT) in black, low-volume 384-well plates (Corning) at room temperature. CTP inhibition assays with yeast-purified CTPS1 and CTPS2 (Fig. 1*A*) were performed with 300 nM CTPS, 200 μM UTP, 600 μM ATP, 30 μM GTP, 100 μM glutamine, and various concentrations of CTP. R80 inhibition assays with yeast-purified CTPS1 (Fig. 5*B*, *SI Appendix*, Fig. S8*A*) were performed with 300 nM CTPS, 200 μM UTP, 600 μM ATP, 30 μM GTP, 100 μM glutamine, and various concentrations of R80. R80 inhibition assays with yeast-purified CTPS2 (Fig. 5*B*, *SI Appendix*, Fig. S8*A*) were performed with 300 nM CTPS, 100 μM UTP, 100 μM ATP, 5 μM GTP, 100 μM glutamine, and various concentrations of R80. Assays had a total volume of 6 μL, and reactions were run for 45 min. The CTPS reaction was terminated by addition of 6 μL ADP-Glo reagent then incubated for 1 h prior to addition of 12 μL kinase detection reagent. After 1 h, luminescence was recorded on a Varioskan Lux (Thermo Scientific) microplate reader. Assays were performed in triplicate. Assays with mouse CTPS and human CTPS purified from Hi5 cells (Figs. 3*A* and 5*C*) were performed at 25 °C in buffer containing 50 mM Hepes, pH 7.4, 10 mM MgCl, 5 mM KCl, 0.01% F-127, and 2 mM DTT. Reactions were performed for 60 min (120 min for CTPS1) and terminated by addition of ADP-Glo reagent for 60 min. Reactions were then incubated with kinase detection reagent for 60 min, after which luminescence was recorded on a Perkin-Elmer Envision 2104 microplate reader. Assay conditions were as follows: 25 or 50 nM CTPS1, 130 μM ATP, 180 μM UTP, 60 μM GTP, 80 μM L-Glutamine; 50 nM CTPS2, 80 μM ATP, 150 μM UTP, 60 μM GTP, 40 μM L-Glutamine; 50 nM mCTPS1, 80 μM ATP, 40 μM UTP, 60 μM GTP, 60 μM L-Glutamine; 50 nM mCTPS2, 30 μM ATP, 30 μM UTP, 60 μM GTP, 80 μM L-Glutamine; 25 nM mCTPS2-I250T, 30 μM ATP, 20 μM UTP, 60 μM GTP, and 120 μM L-Glutamine. Data were fit by four-parameter logistic regression, solving for maximum rate, minimum rate, Hill number, and IC_{50}.

RapidFire Mass-Spectrometry Assays for CTPS Activity. CTPS reactions were carried out in 384-well plates in 50 mM Hepes pH 7.4, 10 mM $MgCl_2$, 5 mM KCl, 2 mM DTT, 0.01% F-127, and 1% dimethyl sulfoxide. Reaction conditions for CTPS1 were as follows: 50 nM CTPS1, 120 μM ATP, 160 μM UTP, 60 μM GTP, 100 μM L-Glutamine, and varying concentrations of inhibitor, as appropriate. Reaction conditions for CTPS2 were as follows: 50 nM CTPS2, 80 μM ATP, 150 μM UTP, 60 μM GTP, 40 μM L-Glutamine, and varying concentrations of inhibitor, as appropriate. Reactions were allowed to proceed at 25 °C for 120 min, prior to the addition of 1% formic acid and 0.5 μM $^{13}C_9{}^{15}N_3$-CTP internal standard (Cambridge Isotope Laboratories Inc.). Calibration standards for CTP concentration were prepared in CTPS1 or CTPS2 reaction buffers. CTP concentrations were measured using a RapidFire Mass-Spectrometry system (Agilent Technologies) using an AB Sciex mass spectrometer.

Negative Stain Electron Microscopy. To prepare samples for negative stain electron microscopy, CTPS was applied to glow-discharged carbon-coated grids and stained with 0.7% uranyl formate. Images were acquired using a Morgagni microscope (FEI) operating at 100 kV and 22,000× magnification on an Orius SC1000 CCD (charge-coupled device) camera (Gatan).

Cryo-EM Sample Preparation and Data Collection. To prepare samples for cryo-EM, CTPS was applied to glow-discharged CFLAT 2/2 holey-carbon grids (Protochips) and blotted away four times successively, before being plunged into liquid ethane using a Vitrobot (ThermoFisher). Sample conditions for CTP-bound CTPS2 were as described previously (10). Conditions for

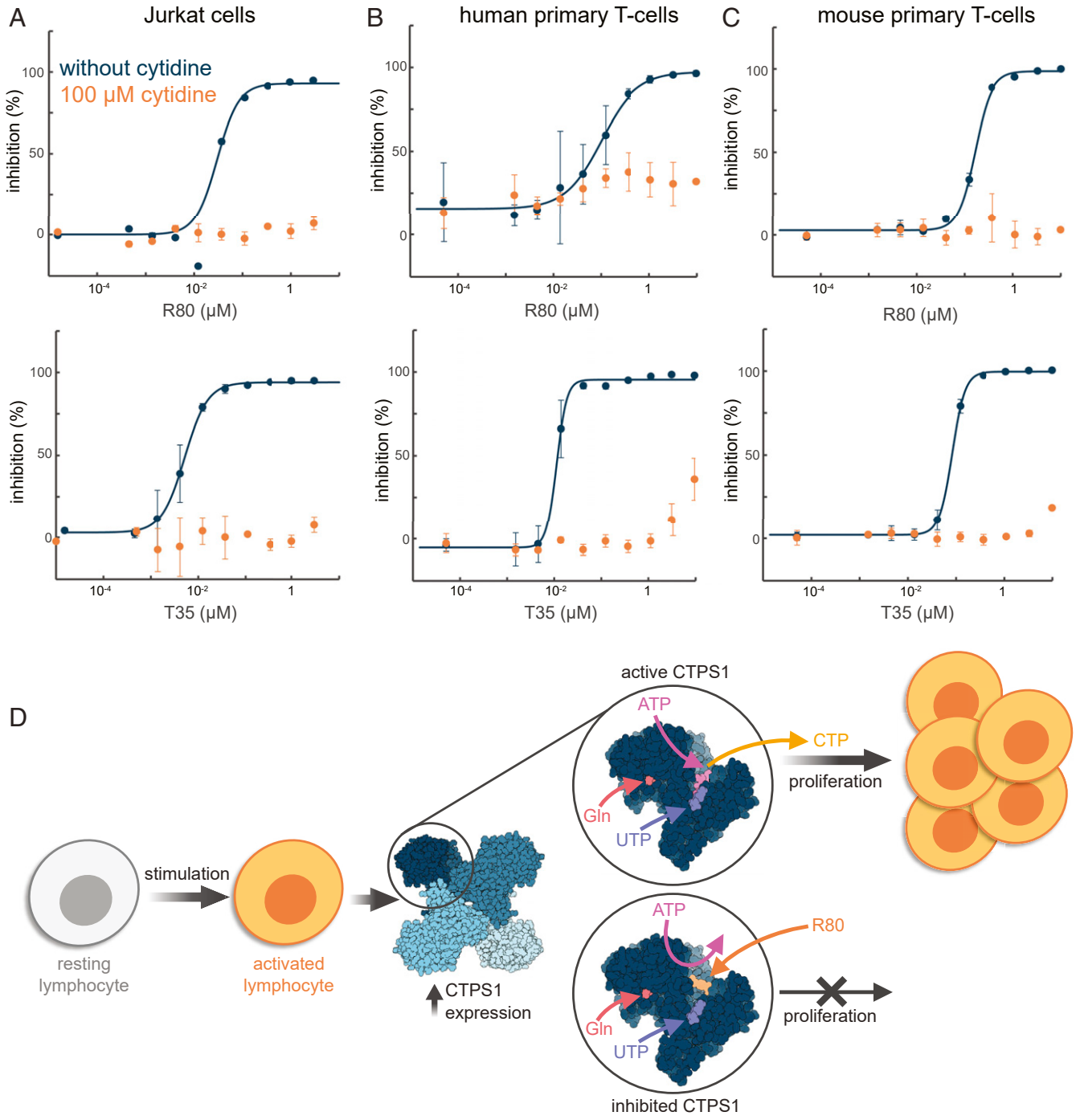

Fig. 6. R80 and T35 inhibit proliferation of cultured lymphocytes. (*A*–*C*) Inhibition of proliferation of jurkat cells (*A*), human primary T cells (*B*), and mouse primary T cells (*C*) in the presence of increasing concentrations of R80 or T35. Inhibition curves without exogenous cytidine (blue) and with 100 μM cytidine (orange) are shown. (*D*) Model: Upon activation, lymphocytes up-regulate CTPS1, leading to increased CTP production from substrates UTP, ATP, and glutamine, allowing for lymphocyte proliferation. Inhibitor R80 prevents binding of ATP to CTPS1, thus inhibiting CTP production and lymphocyte proliferation. Data shown in graphs are mean and SD of $n = 2$ technical replicates from one representative experiment.

CTP-bound CTPS1 were 5 mM CTP and 10 mM $MgCl_2$ in 20 mM Tris · HCl pH 7.9, 100 mM NaCl, and 0.5 mM DTT. Conditions for human and mouse CTPS bound to small molecule inhibitors were 5 μM CTPS, 2 mM UTP, 7.5 mM glutamine, 10 mM $MgCl_2$, and 50 μM R80 or T35 in 20 mM Tris · HCl pH 7.9, 100 mM NaCl, and 0.5 mM DTT. Data for CTP-bound CTPS1 was collected on a Glacios (ThermoFisher). Data for all other structures was collected on a Titan Krios (ThermoFisher) equipped with a Quantum Gatan Imaging Filter energy filter (Gatan Inc.) operating in zero-loss mode with a 20-eV slit width. Both microscopes were equipped with a K-2 Summit Direct Detect camera (Gatan Inc.). On the Glacios, movies were collected in counted mode with a pixel size of 1.16 Å/pixel, with 50 frames and a total dose of 65 electrons/ Å^2. On the Titan Krios, movies were collected in superresolution mode with a pixel size of 0.525 Å/pixel, with 50 frames and a total dose of 90 electrons/ Å^2. Data collection was automated using Leginon (61).

Cryo-EM Data Processing. Workflows for cryo-EM data processing are shown in *SI Appendix* Fig. S3 and S5. Movies were aligned, dose-weighted, and summed using the Relion (62) implementation of MotionCor2 (63). CTF

parameters were estimated using CTFFIND4 (64). Automatic particle picking (using a circular blob reference) and 2-dimensional (2D) classification were performed in cryoSPARC (65). Particles selected from high-quality 2D classes were exported to Relion for 3-dimensional (3D) autorefinement and 3D classification. Relion was also used to perform beamtilt, anisotropic magnification, and defocus refinement, as well as Bayesian particle polishing. For filament samples, Relion signal subtraction was performed following Bayesian polishing, leaving signal for only a central tetramer. Finally, density modification was performed using ResolveCryoEM in Phenix (66, 67).

Model Building, Refinement, and Ligand Placement. Preliminary models of the CTPS1 and CTPS2 dimers were built using Protein Data Bank (PDB) IDs 5U03 and 6PK4, respectively. Initial homology models of mCTPS1 and mCTPS2 were generated with Modeler (68), using PDB 6PK4 as a reference. Models were docked into the cryo-EM maps as rigid bodies using Chimera (69), and initial refinement into the cryo-EM density was performed with Isolde (70). UTP nucleotides, magnesium ions, free glutamine residues, and either the R80 or T35 ligand were modeled in each CTPS polypeptide, and the structures were manually inspected to adjust sidechain rotamers and rebuild poorly resolved loops near the binding sites with Coot (71). Structures were prepared for further refinement with Schrödinger's Protein Preparation Wizard (72). For each structure, bond orders were assigned, hydrogen atoms were added, metal zero-order bonds created, and ligand protonation and tautomer states were assigned (73, 74), followed by hydrogen bond network optimization (pH set to 7.4) and a restrained energy minimization of only the hydrogens. To minimize overfitting during refinement with Phenix/OPLS3e, a scan of the phenix.real_space_refine weight parameter was performed using Schrödinger's phenix_weight_scan.py utility (25, 75). Phenix/OPLS3e uses the OPLS3e force field (76) and VSGB2.1 solvation model (77) to calculate energies and gradients. To reduce local overfitting, ligand energy was monitored against the local map-model correlation as a function of the weight factor, and final weights were determined such that ligand energy values were no more than 1 log unit (10 kcal/mol) greater than that observed for the lowest energy conformer. The same weights were tested for each structure (0.1, 0.2, 0.5, 1.0, 2.0, 3.0, 4.0, 5.0, 8.0, and 10.0), and the optimal weights were selected independently for each structure (CTPS1_R80 = 0.5, CTPS2_R80 = 2.0, CTPS1_T35 = 2.0, CTPS2_T35 = 1.0, mCTPS1_R80 = 1.0, mCTPS2_R80 = 0.5, and mCTPS2_I250T_R80 = 2.0). The structure models were then passed as inputs to GlideEM (24), which redocked the R80/T35 ligands. Top-scoring candidate poses were then subjected to a round of real-space refinement in Phenix/OPLS3e using the previously optimized weight factors and otherwise default parameters, and the optimal pose for each ligand-bound structure was selected (25). A final round of real space refinement in Phenix/OPLS3e was then performed through Schrodinger's phenix.py interface, using additional noncrystallographic symmetry restraints on the two CTPS polypeptide chains, followed by a final round of Protein Preparation Wizard to reoptimize hydrogen bond networks. All Schrödinger tools used the 2020-3 suite for calculations, and version 1.18.2 was used for Phenix. Cryo-EM data collection, refinement, and validation statistics are summarized in *SI Appendix*, Table S3.

Jurkat Cell Proliferation Assays. Jurkat cells (ATCC TIB152) were grown in Roswell Park Memorial Institute (RPMI) 1640 media containing 10% fetal bovine serum (FBS) and 1% penicillin/streptomycin at 37 °C and 5% CO_2 for 5 d in 96-well plates. Cells were grown in the presence of various concentrations of R80 or T35 with or without 100 μM cytidine, as appropriate. An equal volume of CellTiter-Glo (CTG) reagent (Promega) was added to cells and incubated at room temperature for 30 min. Cell viability was measured by recording luminescence using a Perkin-Elmer Envision microplate reader.

Primary T Cell Proliferation Assays. Assays with human primary T cells were conducted by Pharmaron. Human peripheral blood mononuclear cells for these assays were sourced commercially from Sailybio (Cat. No. SLB-HP200A), with ethical approvals and informed consent for the collection. Human primary T cells were isolated from fresh peripheral blood mononuclear cells (Sailybio) using the human Pan T Cell Isolation Kit (Miltenyi Biotec) and resuspended in RPMI medium 1640 containing 10% FBS, 1% penicillin/streptomycin, and 10 ng/mL human IL-2 (R&D Systems). Mouse primary T cells were isolated from fresh spleen cells using the mouse Pan T Cell Isolation Kit (Miltenyi Biotec) and resuspended in RPMI medium 1640 containing 10% FBS, 1% penicillin/streptomycin, and 10 ng/mL mouse IL-2 (R&D Systems). Compounds R80 and T35 were added as appropriate to various concentrations. Cells were seeded into 96-well plates and incubated at 37 °C and 5% CO_2 for 1 h. Human or mouse anti-CD3/anti-CD28 Dynabeads (Thermo Fisher Scientific) (78) and 100 μM cytidine (where appropriate) were then added, and cells were incubated at 37 °C and 5% CO_2 for 5 d. CTG reagent (Promega) was added to cells and incubated at room temperature for 30 min, after which luminescence was recorded using a Perkin-Elmer Envision microplate reader.

Data Availability. Cryo-EM structures and atomic models have been deposited in the Electron Microscopy Data Bank (EMDB) and PDB, respectively, with the following accession codes: EMD-23831, PDB: 7MGZ (CTPS1 bound to AMPPNP, UTP, and glutamine); EMD-23832, PDB: 7MH0 (CTPS1 bound to CTP); EMD-23848, PDB: 7MIF (CTPS1 bound to R80); EMD-23850, PDB: 7MIG (CTPS1 bound to T35); EMD-23833, PDB: 7MH1 (CTPS2 bound to CTP); EMD-23851, PDB: 7MIH (CTPS2 bound to R80); EMD-23852, PDB: 7MII (CTPS2 bound to T35); EMD-23859, PDB: 7MIP (mCTPS1 bound to R80); EMD-23865, PDB: 7MIU (mCTPS2 bound to R80); EMD-23866, PDB: 7MIV (mCTPS2-I250T bound to R80).

ACKNOWLEDGMENTS. We thank the Arnold and Mabel Beckman Cryo-EM Center at the University of Washington for the use of electron microscopes. This work was supported NIH Grants R01 GM118396, R01 AI153048, and S10 OD032290 to J.M.K. and Grant T32 GM007270 to J.M.H.

1. E. Martin *et al.*, CTP synthase 1 deficiency in humans reveals its central role in lymphocyte proliferation. *Nature* **510**, 288–292 (2014).
2. E. Martin *et al.*; Genomics England Research Consortium, Impaired lymphocyte function and differentiation in CTPS1-deficient patients result from a hypomorphic homozygous mutation. *JCI Insight* **5**, e133880 (2020).
3. L. D. Fairbanks, M. Bofill, K. Ruckemann, H. A. Simmonds, Importance of ribonucleotide availability to proliferating T-lymphocytes from healthy humans. Disproportionate expansion of pyrimidine pools and contrasting effects of de novo synthesis inhibitors. *J. Biol. Chem.* **270**, 29682–29689 (1995).
4. G. Falkson *et al.*, A randomized phase II study of acivicin and 4'deoxydoxorubicin in patients with hepatocellular carcinoma in an Eastern Cooperative Oncology Group study. *Am. J. Clin. Oncol.* **13**, 510–515 (1990).
5. I. N. Olver, M. Green, M. J. Millward, J. F. Bishop, Phase II study of acivicin in patients with recurrent high grade astrocytoma. *J. Clin. Neurosci.* **5**, 46–48 (1998).
6. J. A. Endrizzi, H. Kim, P. M. Anderson, E. P. Baldwin, Crystal structure of *Escherichia coli* cytidine triphosphate synthetase, a nucleotide-regulated glutamine amidotransferase/ATP-dependent amidoligase fusion protein and homologue of anticancer and antiparasitic drug targets. *Biochemistry* **43**, 6447–6463 (2004).
7. J. A. Endrizzi, H. Kim, P. M. Anderson, E. P. Baldwin, Mechanisms of product feedback regulation and drug resistance in cytidine triphosphate synthetases from the structure of a CTP-inhibited complex. *Biochemistry* **44**, 13491–13499 (2005).
8. C. Habrian *et al.*, Inhibition of *Escherichia coli* CTP synthetase by NADH and other nicotinamides and their mutual interactions with CTP and GTP. *Biochemistry* **55**, 5554–5565 (2016).
9. E. M. Lynch *et al.*, Human CTP synthase filament structure reveals the active enzyme conformation. *Nat. Struct. Mol. Biol.* **24**, 507–514 (2017).
10. E. M. Lynch, J. M. Kollman, Coupled structural transitions enable highly cooperative regulation of human CTPS2 filaments. *Nat. Struct. Mol. Biol.* **27**, 42–48 (2020).
11. G. D. McCluskey, S. L. Bearne, "Pinching" the ammonia tunnel of CTP synthase unveils coordinated catalytic and allosteric-dependent control of ammonia passage. *Biochim. Biophys. Acta, Gen. Subj.* **1862**, 2714–2727 (2018).
12. R. M. Barry *et al.*, Large-scale filament formation inhibits the activity of CTP synthetase. *eLife* **3**, e03638 (2014).
13. X. Zhou *et al.*, Drosophila CTP synthase can form distinct substrate- and product-bound filaments. *J. Genet. Genomics* **46**, 537–545 (2019).
14. W. C. Carcamo *et al.*, Induction of cytoplasmic rods and rings structures by inhibition of the CTP and GTP synthetic pathway in mammalian cells. *PLoS One* **6**, e29690 (2011).
15. T. I. Strochlic *et al.*, Ack kinase regulates CTP synthase filaments during Drosophila oogenesis. *EMBO Rep.* **15**, 1184–1191 (2014).
16. I. Petrovska *et al.*, Filament formation by metabolic enzymes is a specific adaptation to an advanced state of cellular starvation. *eLife* **3**, e02409 (2014).
17. G. N. Aughey *et al.*, Nucleotide synthesis is regulated by cytoophidium formation during neurodevelopment and adaptive metabolism. *Biol. Open* **3**, 1045–1056 (2014).
18. S. J. Calise *et al.*, Glutamine deprivation initiates reversible assembly of mammalian rods and rings. *Cell. Mol. Life Sci.* **71**, 2963–2973 (2014).
19. X. Zhou *et al.*, Structural basis for ligand binding modes of CTP synthase. *Proc. Natl. Acad. Sci. U.S.A.* **118**, e2026621118 (2021).
20. A. Quddus *et al.*, N-(4-(5-chloropyridin-3-yl)phenyl)-2-(2-(cyclopropanesulfonamido) pyrimidin-4-yl) butanamide derivatives and related compounds as human CTPS1 inhibitors for the treatment of proliferative diseases. World Patent 2020245665 (2020).
21. A. Quddus *et al.*, Aminopyrimidine derivatives as CTPS1 inhibitors. World Patent 2019179652 (2019).
22. A. Quddus *et al.*, Compounds. World Patent 2019106156 (2019).
23. A. Novak *et al.*, Compounds. World Patent 2019106146 (2019).
24. M. J. Robertson, G. C. P. van Zundert, K. Borrelli, G. Skiniotis, GemSpot: A pipeline for robust modeling of ligands into cryo-EM maps. *Structure* **28**, 707–716.e3 (2020).

25. G. C. P. van Zundert, N. W. Moriarty, O. V. Sobolev, P. D. Adams, K. W. Borrelli, Macromolecular refinement of X-ray and cryoelectron microscopy structures with Phenix/OPLS3e for improved structure and ligand quality. *Structure* **29**, 913–921.e4 (2021).
26. J. J. Gu *et al*., Inhibition of T lymphocyte activation in mice heterozygous for loss of the IMPDH II gene. *J. Clin. Invest.* **106**, 599–606 (2000).
27. M. Nagai, Y. Natsumeda, G. Weber, Proliferation-linked regulation of type II IMP dehydrogenase gene in human normal lymphocytes and HL-60 leukemic cells. *Cancer Res.* **52**, 258–261 (1992).
28. M. Senda, Y. Natsumeda, Tissue-differential expression of two distinct genes for human IMP dehydrogenase (E.C.1.1.1.205). *Life Sci.* **54**, 1917–1926 (1994).
29. Y. Natsumeda *et al*., Two distinct cDNAs for human IMP dehydrogenase. *J. Biol. Chem.* **265**, 5292–5295 (1990).
30. R. C. Jackson, G. Weber, H. P. Morris, IMP dehydrogenase, an enzyme linked with proliferation and malignancy. *Nature* **256**, 331–333 (1975).
31. M. C. Johnson, J. M. Kollman, Cryo-EM structures demonstrate human IMPDH2 filament assembly tunes allosteric regulation. *eLife* **9**, e53243 (2020).
32. G. D. Keppeke *et al*., IMP/GTP balance modulates cytoophidium assembly and IMPDH activity. *Cell Div.* **13**, 5 (2018).
33. K. Wolfe *et al*., Dynamic compartmentalization of purine nucleotide metabolic enzymes at leading edge in highly motile renal cell carcinoma. *Biochem. Biophys. Res. Commun.* **516**, 50–56 (2019).
34. S. J. Calise, G. Abboud, H. Kasahara, L. Morel, E. K. L. Chan, Immune Response-Dependent Assembly of IMP Dehydrogenase Filaments, Immune response-dependent assembly of IMP dehydrogenase filaments. *Front. Immunol.* **9**, 2789 (2018).
35. K. C. Duong-Ly *et al*., T cell activation triggers reversible inosine-5′-monophosphate dehydrogenase assembly. *J. Cell Sci.* **131**, jcs223289 (2018).
36. J. C. Williams, H. Kizaki, G. Weber, H. P. Morris, Increased CTP synthetase activity in cancer cells. *Nature* **271**, 71–73 (1978).
37. P. H. Ellims, T. E. Gan, G. Medley, Cytidine triphosphate synthetase activity in lymphoproliferative disorders. *Cancer Res.* **43**, 1432–1435 (1983).
38. A. C. Verschuur, A. H. van Gennip, E. J. Muller, P. A. Voûte, A. B. P. van Kuilenburg, Increased activity of cytidine triphosphate synthetase in pediatric acute lymphoblastic leukemia. *Clin. Biochem.* **30**, 292 (1997).
39. M. S. Lui, H. Kizaki, G. Weber, Biochemical pharmacology of acivicin in rat hepatoma cells. *Biochem. Pharmacol.* **31**, 3469–3473 (1982).
40. G. Weber *et al*., Control of enzymic programs and nucleotide pattern in cancer cells by acivicin and tiazofurin. *Adv. Enzyme Regul.* **22**, 69–93 (1984).
41. J. Oliveira de Souza, A. Dawson, W. N. Hunter, An improved model of the Trypanosoma brucei CTP synthetase glutaminase domain-acivicin complex. *ChemMedChem* **12**, 577–579 (2017).
42. K. Gharehbaghi, W. Zhen, M. Fritzer-Szekeres, T. Szekeres, H. N. Jayaram, Studies on the antitumor activity and biochemical actions of cyclopentenyl cytosine against human colon carcinoma HT-29 in vitro and in vivo. *Life Sci.* **64**, 103–112 (1999).
43. A. C. Verschuur, A. H. Van Gennip, R. Leen, P. A. Voûte, A. B. P. Van Kuilenburg, "Cyclopentenyl cytosine induces apoptosis and secondary necrosis in a T-lymphoblastic leukemic cell-line" in *Purine and Pyrimidine Metabolism in Man X*, E. Zoref-Shani, O. Sperling, Eds. (Springer US, 2002), pp. 319–325.
44. M. C. Wang, A. Bloch, Studies on the mode of action of 3-deazapyrimidines. 1. Metabolism of 3-deazauridine and 3-deazacytidine in microbial and tumor cells. *Biochem. Pharmacol.* **21**, 1063–1073 (1972).
45. R. P. McPartland, M. C. Wang, A. Bloch, H. Weinfeld, Cytidine 5′-triphosphate synthetase as a target for inhibition by the antitumor agent 3-deazauridine. *Cancer Res.* **34**, 3107–3111 (1974).
46. R. W. Brockman *et al*., The mechanism of action of 3-deazauridine in tumor cells sensitive and resistant to arabinosylcytosine. *Ann. N. Y. Acad. Sci.* **255**, 501–521 (1975).
47. J. Bierau *et al*., Cyclopentenyl cytosine primes SK-N-BE(2)c neuroblastoma cells for cytarabine toxicity. *Int. J. Cancer* **103**, 387–392 (2003).
48. A. C. Verschuur *et al*., Cyclopentenyl cytosine increases the phosphorylation and incorporation into DNA of 1-β-D-arabinofuranosyl cytosine in a human T-lymphoblastic cell line. *Int. J. Cancer* **98**, 616–623 (2002).
49. A. C. Verschuur, A. H. Van Gennip, R. Leen, A. B. P. Van Kuilenburg, Increased cytotoxicity of 2′,2′-difluoro-2′-deoxycytidine in human leukemic cell-lines after a preincubation with cyclopentenyl cytosine. *Nucleosides Nucleotides Nucleic Acids* **23**, 1517–1521 (2004).
50. S. M. Blaney *et al*., Mechanism of resistance to cyclopentenyl cytosine (CPE-C) in Molt-4 lymphoblasts. *Biochem. Pharmacol.* **45**, 1493–1501 (1993).
51. H. Zhang *et al*., Resistance to cyclopentenylcytosine in murine leukemia L1210 cells. *Cancer Res.* **53**, 5714–5720 (1993).
52. N. Dereuddre-Bosquet *et al*., Inhibitors of CTP biosynthesis potentiate the anti-human immunodeficiency virus type 1 activity of 3TC in activated peripheral blood mononuclear cells. *Antiviral Res.* **61**, 67–70 (2004).
53. Y. Rao *et al*., Targeting CTP synthetase 1 to restore interferon induction and impede nucleotide synthesis in SARS-CoV-2 infection. *bioRxiv* (2021) https://doi.org/10.1101/2021.02.05.429959. Accessed 1 August 2021.
54. B. A. Webb, A. M. Dosey, T. Wittmann, J. M. Kollman, D. L. Barber, The glycolytic enzyme phosphofructokinase-1 assembles into filaments. *J. Cell Biol.* **216**, 2305–2313 (2017).
55. S. A. Anthony *et al*., Reconstituted IMPDH polymers accommodate both catalytically active and inactive conformations. *Mol. Biol. Cell* **28**, 2600–2608 (2017).
56. C. Noree *et al*., A quantitative screen for metabolic enzyme structures reveals patterns of assembly across the yeast metabolic network. *Mol. Biol. Cell* **30**, 2721–2736 (2019).
57. D. G. Roth, E. Shelton, T. F. Deuel, Purification and properties of phosphoribosyl pyrophosphate synthetase from rat liver. *J. Biol. Chem.* **249**, 291–296 (1974).
58. J.-P. Renaud *et al*., Cryo-EM in drug discovery: Achievements, limitations and prospects. *Nat. Rev. Drug Discov.* **17**, 471–492 (2018).
59. J. H. Van Drie, L. Tong, Cryo-EM as a powerful tool for drug discovery. *Bioorg. Med. Chem. Lett.* **30**, 127524 (2020).
60. G.-S. Han *et al*., Expression of human CTP synthetase in Saccharomyces cerevisiae reveals phosphorylation by protein kinase A. *J. Biol. Chem.* **280**, 38328–38336 (2005).
61. C. Suloway *et al*., Automated molecular microscopy: The new Leginon system. *J. Struct. Biol.* **151**, 41–60 (2005).
62. S. H. W. Scheres, RELION: Implementation of a Bayesian approach to cryo-EM structure determination. *J. Struct. Biol.* **180**, 519–530 (2012).
63. S. Q. Zheng *et al*., MotionCor2: Anisotropic correction of beam-induced motion for improved cryo-electron microscopy. *Nat. Methods* **14**, 331–332 (2017).
64. A. Rohou, N. Grigorieff, CTFFIND4: Fast and accurate defocus estimation from electron micrographs. *J. Struct. Biol.* **192**, 216–221 (2015).
65. A. Punjani, J. L. Rubinstein, D. J. Fleet, M. A. Brubaker, cryoSPARC: Algorithms for rapid unsupervised cryo-EM structure determination. *Nat. Methods* **14**, 290–296 (2017).
66. T. C. Terwilliger, S. J. Ludtke, R. J. Read, P. D. Adams, P. V. Afonine, Improvement of cryo-EM maps by density modification. *Nat. Methods* **17**, 923–927 (2020).
67. P. D. Adams *et al*., PHENIX: A comprehensive Python-based system for macromolecular structure solution. *Acta Crystallogr. D Biol. Crystallogr.* **66**, 213–221 (2010).
68. B. Webb, A. Sali, Comparative protein structure modeling using MODELLER. *Curr. Protoc. Bioinformatics* **54**, 5.6.1–5.6.37 (2016).
69. E. F. Pettersen *et al*., UCSF Chimera—A visualization system for exploratory research and analysis. *J. Comput. Chem.* **25**, 1605–1612 (2004).
70. T. I. Croll, ISOLDE: A physically realistic environment for model building into low-resolution electron-density maps. *Acta Crystallogr. D Struct. Biol.* **74**, 519–530 (2018).
71. P. Emsley, B. Lohkamp, W. G. Scott, K. Cowtan, Features and development of Coot. *Acta Crystallogr. D Biol. Crystallogr.* **66**, 486–501 (2010).
72. G. M. Sastry, M. Adzhigirey, T. Day, R. Annabhimoju, W. Sherman, Protein and ligand preparation: Parameters, protocols, and influence on virtual screening enrichments. *J. Comput. Aided Mol. Des.* **27**, 221–234 (2013).
73. J. C. Shelley *et al*., Epik: A software program for pK(a) prediction and protonation state generation for drug-like molecules. *J. Comput. Aided Mol. Des.* **21**, 681–691 (2007).
74. J. R. Greenwood, D. Calkins, A. P. Sullivan, J. C. Shelley, Towards the comprehensive, rapid, and accurate prediction of the favorable tautomeric states of drug-like molecules in aqueous solution. *J. Comput. Aided Mol. Des.* **24**, 591–604 (2010).
75. P. V. Afonine *et al*., Real-space refinement in PHENIX for cryo-EM and crystallography. *Acta Crystallogr. D Struct. Biol.* **74**, 531–544 (2018).
76. K. Roos *et al*., OPLS3e: Extending force field coverage for drug-like small molecules. *J. Chem. Theory Comput.* **15**, 1863–1874 (2019).
77. J. Li *et al*., The VSGB 2.0 model: A next generation energy model for high resolution protein structure modeling. *Proteins* **79**, 2794–2812 (2011).
78. A. Trickett, Y. L. Kwan, T cell stimulation and expansion using anti-CD3/CD28 beads. *J. Immunol. Methods* **275**, 251–255 (2003).